ADVANCED FUNCTIONAL MATERIALS
www.afm-journal.de

Fluorophobic Effect Enables Selective Detection of PFAS in Water with Electrolyte-Gated Organic Transistors

Rian Zanotti, Marcello Berto, Matteo Sensi, Alessandro Paradisi, Eleonora Veronese, Lucia Pasquato, Carlo Augusto Bortolotti, Pierangelo Metrangolo, and Fabio Biscarini**

PerFluoroAlkyl Substances (PFAS) are responsible of major environmental pollution worldwide, as they are both persistent and mobile. Environmental agencies impose strict regulations about PFAS in drinking water, hence, there is an urgent need for on-field deployable, rapid, reproducible, and distributed monitoring of PFAS. This work demonstrates an ultra-sensitive sensor for perfluoroalkyl acids based on an organic transistor whose gate is functionalized with a binary self-assembled monolayer containing a perfluorinated molecule. The device exploits the fluorophobic effect for selectively recognizing different PFAS based on the different number of fluorous interactions, *viz*. fluorine-fluorine (F···F) contacts, that can be formed. Remarkably, the organic transistor senses differences in the binding energy to linear PFAS surfactants in water of 4 ± 1 kJ mol^{-1}, which corresponds to one —CF_2- unit. This device allows to quantify PFAS in water down to ppt level of detection.

1. Introduction

PerFluoroAlkyl Substances (PFAS) are a family of persistent organic pollutants with a variety of structural, physico-chemical, and toxicological properties,[1] which are currently raising global concern for environment and health. Two of the most harmful PFAS are PerFluoroOctanoic Acid (PFOA) and PerFluoroOctyl Sulfonate (PFOS), both entailing a perfluoroalkyl chain bound to a carboxylic and a sulfonic acid group, respectively. These molecules have been linked to cancer and other health problems,[2–4] and are responsible for major environmental pollution worldwide due to their long-range transport and persistence linked to the strength of the C—F covalent bond.[5,6]

The wide diffusion and the demonstrated effects of PFAS on human health forced national and international organizations to adopt new regulations that introduce more stringent limits for their concentration in drinking water and food. The revised EU Drinking Water Directive in 2020 introduced two relevant parameters for water legislation starting from 2025: The limit for the "sum of PFAS" of 0.1 µg L^{-1}, which regards a list of 20 PFAS, among them PFOA, PFOS, PerFluoroNonanoic Acid, and PerFluoroHexane Sulfonate (PFHxS),[7] and the limit of "total PFAS" of 0.5 µg L^{-1}, which refers to the entire PFAS family that, according to the OECD recommendation, may group some 10 000 compounds.[8] Other organizations, like the United States Environmental Protection Agency (US-EPA), suggest much more stringent concentration limits for each single PFAS in the order of ppt and even below (PFOA: 0.004 ppt; PFOS: 0.02 ppt).[9,10]

At the state of the art, the golden analytical technique for PFAS detection in water, which enables to achieve limits of detection (LODs) suitable for the regulated parameters, is liquid chromatography coupled with tandem mass spectrometry. It is a consolidated, highly precise technique, but requires expensive laboratory instrumentation operated by trained personnel. Furthermore, the managing of new molecules requires new standards, and the technique is not deployable on field and is time consuming.[11] A laboratory approach alone is not sufficient for covering the needs of monitoring and mapping the territory and the waters affected by PFAS pollution. There is, indeed, an unmet need for in-field deployable platforms for PFAS detection that exhibit the following requirements:[12] i) small, portable, easy

R. Zanotti, M. Berto, M. Sensi, A. Paradisi, C. A. Bortolotti, F. Biscarini
Department of Life Sciences
University of Modena and Reggio Emilia
Via Giuseppe Campi 103, Modena 41125, Italy
E-mail: marcello.berto@unimore.it; fabio.biscarini@unimore.it
R. Zanotti
Department of Physics, Informatics and Mathematics
University of Modena and Reggio Emilia
Via Campi 213/a, Modena 41125, Italy
E. Veronese, C. A. Bortolotti, P. Metrangolo
Department of Chemistry, Materials and Chemical Engineering "Giulio Natta"
Politecnico di Milano
via L. Mancinelli 7, Milan 20131, Italy
L. Pasquato
Department of Chemical and Pharmaceutical Sciences
University of Trieste
Via Licio Giorgieri 1, Trieste 34127, Italy
F. Biscarini
Center for Translational Neurophysiology of Speech and Communication
Istituto Italiano di Tecnologia (CTNSC)
Via Fossato di Mortara 17-19, Ferrara 44121, Italy

The ORCID identification number(s) for the author(s) of this article can be found under https://doi.org/10.1002/adfm.202508425

DOI: 10.1002/adfm.202508425

to use, and inexpensive; ii) specific and selective; iii) LODs in the range of sub-ppt for most of the PFAS.

Different approaches were proposed for PFAS monitoring: colorimetric sensors with nanoparticles functionalized with perfluorinated SAMs;[13,14] impedentiometric sensors with molecularly imprinted polymers or metal organic framework as PFAS recognition elements;[15,16] DNA aptasensors coupled to fluorescence detection;[17] amplifying fluorescent polymers,[18] among others. Recently, a detection limit of 400 ppt for PFOA was attained by measuring resistivity changes in an electrical lateral flow sensor.[19] However, the reported LODs do not satisfy current legislation requirements. To the best of our knowledge, there are no examples of PFAS sensors using Electrolyte Gated Organic Transistors (EGOTs), albeit EGOT ultra-sensitivity is widely documented in the literature,[20–23] down to the detection of single molecule recognition events.[24]

In this work, we report the first example of an EGOT capable of specific and selective interactions with PFAS at a solid/water interface. It features a label-free architecture that specifically recognizes and quantifies perfluoroalkyl acids, whose chain length is four, six, and eight carbon atoms, i.e., PerFluoroButanoic Acid (PFBA), PerFluoroHexanoic Acid (PFHxA), and PFOA, with record-low LODs of 11.9 pM (2.5 ppt), 3.9 pM (1.2 ppt), and 97 fM (0.04 ppt), respectively, discriminating one from the other. The device exploits functionalization of the EGOT gate electrode with a mixed self-assembled monolayer (SAM) that includes 1H,1H,2H,2H-perfluorodecanethiol (PFDT) and a majority mercapto-oligoethylene glycol (OEG). PFDT exhibits a high fluorous affinity for the target PFAS. The capacitive coupling between the gate electrode and the organic semiconductor channel (OSC) amplifies the effects of the interfacial PFAS/mixed SAMs interaction. Fluorophobic effect and the consequent electrostatic interfacial interactions are then transduced into the transfer current curves of the EGOT, showing that its selectivity toward the tested PFAS is due to an increase of the effective association constant, corresponding to a difference in binding free energy in the order of less than 2 RT (4 kJ mol^{-1}) per -CF_2- unit. Control experiments confirm the "transparency" of a non-fluorinated surfactant to the perfluoro-functionalized EGOT sensor. Hence, the EGOT sensor responds selectively to noncovalent interactions of the same nature, *viz*. fluorous, resolving differences in the order of thermal energy amongst chemically and structurally similar molecules. Our EGOT design fosters exploitation of multiple F···F interactions as a viable strategy enabling selective PFAS recognition by exploiting the electronic amplification of minute differences in the electrostatic interactions at the EGOT gate/water interface between the perfluorinated probe molecules and the PFAS.

2. Results and Discussion

We demonstrate how our gate-functionalized EGOT is able to sense the target PFAS in aqueous solution. The device exploits fluorine-fluorine interactions, also known as fluorophobic effect,[25] between the PFAS and a mixed OEG/PFDT Self-Assembled Monolayer (SAM) deposited on the Au gate electrode surface. The sensitivity and selectivity toward different PFAS, specifically these three substances with perfluorinated chains of increasing length, is imparted by the number of F···F interactions and the capability of the EGOT response to resolve weak interactions in the order of a few kJ mol^{-1} units.

First, we show how the device is made highlighting the molecular model for the functionalized gate electrode. Then, we discuss how the interaction between the SAM and the target analytes changes the multiparametric response of the EGOT device, and we assess the steady-state response of the EGOT to increasing concentrations of different PFAS (and some relevant controls) in water. Afterward, we analyze the current variation due to the interaction between the sensor and the analytes comparing a canonic linear model of the EGOT, and a novel model that we recently proposed for describing the whole transfer response of the EGOT including the electronic properties of the organic channel.[26] Finally, we estimate the LOD and the sensitivity, and discuss, through the binding free energy, the impact of the fluorophobic effect in imparting the EGOT exquisite sensitivity and chemical selectivity based on noncovalent fluorine-fluorine interactions.

2.1. Functionalization of the Gate Electrode with Mixed SAM

The EGOT exhibits a three-electrode architecture (source, drain, and gate) where the semiconductor channel between source and drain is capacitively coupled to the gate electrode through the electrolyte (distilled water in this work). The device layout is depicted in **Figure 1a**. The sensitivity of the EGOT toward the PFAS arises from the functionalization of the gate electrode with a mixed SAM obtained by its overnight incubation in an ethanol solution of 1H,1H,2H,2H-PFDT and 2-[2-[2-(2-methoxyethoxy)ethoxy]ethoxy]ethanethiol, a thiol four unit-long OEG (Figure 1b).[27] The mixed-SAM was designed with the aim to: i) minimize nonspecific interactions with small biomolecules eventually present in relevant water samples; ii) favor the wettability of the electrode surface by aqueous solutions by tuning the OEG/PFDT ratio; iii) promote the segregation of the minority component PFDT within the OEG matrix to maximize the interface for PFAS molecular recognition.[28,29]

The system is considered to attain equilibrium, hence the surface concentration and the surface distribution of each species in the mixed SAM will be time-invariant, as suggested by the fact that we did not observe a substantial continuous drift of the EGOT characteristics. The mixed SAM likely consists of phase-segregated domains of the minority PDFT molecules embedded into a continuous 2D matrix of the OEG (Figure 1b).[30–32] We assume that the same 1:3 ratio of PFDT:OEG in solution is also reflected in the SAM composition. The PFDT domains are expected to establish interactions with the PFAS in the aqueous solution, while the OEG forms a smooth and compact 2D diffusional barrier for the PFAS. On the one hand, this feature protects the electrode from nonspecific PFAS adsorption on the Au surface and, on the other hand, it enables surface diffusion of the PFAS until they reach the binding sites in the PFDT domains. Thus, we envision that in an optimum EGOT sensor, the characteristic distance (correlation length) between PFDT domains should be comparable to half the surface diffusion length of PFAS onto the OEG SAM.

We assess the overall SAM coverage with Electrochemical Impedance Spectroscopy (EIS) and Cyclic Voltammetry (CV),

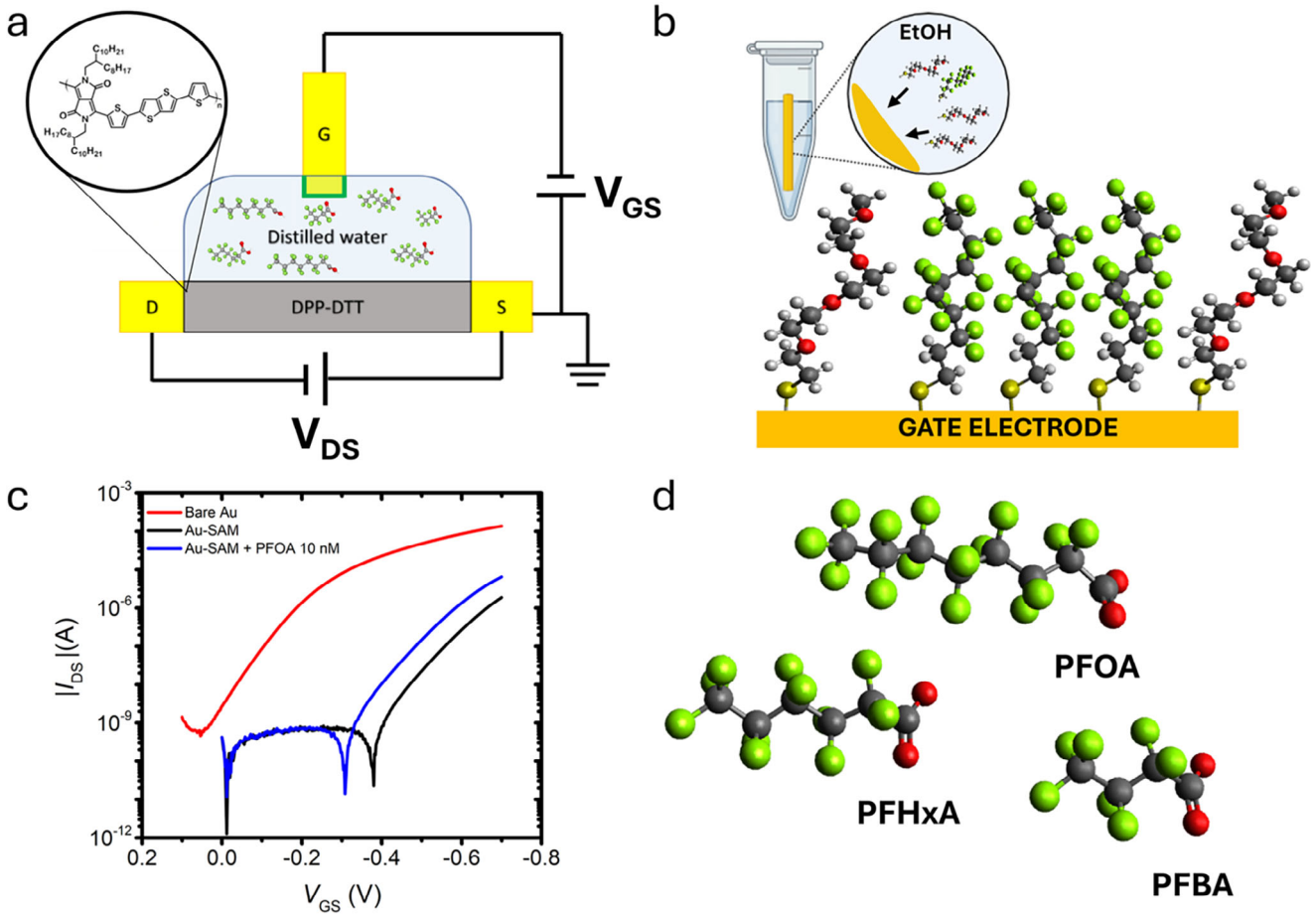

Figure 1. a) Schematic drawing of the PFAS EGOT sensor; inset: structure of the DPP-DTT semiconductor. b) Schematic representation of the mixed SAM. F atoms are depicted in green, O in red, C in gray, S in yellow, and H in white. The drawing on the top left depicts the functionalization of the Au gate electrode incubated in an ethanol binary solution of PFDT and OEG. c) Transfer curves recorded with bare gold (red), SAM-functionalized gold (black) gate electrode, and the latter after exposure to a 10 nM solution of PFOA (blue). d) molecular structures of the three linear PFAS target molecules.

both confirming that incubation yielded complete coverage of the whole Au surface, since a decrease of the redox current associated with the oxidation and reduction of an electrochemical probe in CV and an increase of the electron transfer resistance in the electrochemical impedance (EIS) spectrum are observed, as shown in Figure S1 (Supporting Information). The comparison of the results of electrochemical characterization of different functionalized electrodes proved that the functionalization protocol is highly reproducible.

2.2. The EGOT Sensor

The EGOT device depicted in Figure 1a features a 24 ± 8 nm-thin film of poly[2,5-(2-octyldodecyl)-3,6-diketopyrrolopyrrole-alt-5,5-(2,5-di(thien-2-yl)thieno[3,2-b]thiophene)] (DPP-DTT) (its chemical structure is shown in the **inset of** Figure 1a) spin cast to form the semiconducting channel. The DPP-DTT thin film exhibits a smooth and homogeneous morphology, with <50 nm diameter grains forming a compact continuous coating (Figure S2, Supporting Information).[33] The gate electrode is negatively polarized to accumulate positive charge carriers in the *p*-type DPP-DTT channel, and a negative potential difference V_{DS} is applied between the source and drain to drive the I_{DS} channel current.

In the linear regime, the channel current can be described as:

$$I_{DS} = \frac{W}{L}\mu C_{eff}\left(V_{GS} - V_{th}\right)V_{DS} \quad (1)$$

where the geometric parameter W/L is the ratio between the channel width W and the length L, the effective capacitance C_{eff} generates the charge carriers upon the application of a nonzero V_{GS}–V_{th}, and μ is the charge carrier mobility in the channel. The threshold voltage V_{th} embodies the electrostatic field within the organic semiconductor that can be generated by adventitious dopants or capacitively induced charges. The transfer curves (Figure 1c) were acquired by fixing V_{DS} = –0.1 V while sweeping V_{GS} from 0 to –0.7 V and back. Figure 1c shows the apparent decrease of I_{DS} after the functionalization of the gate electrode. Also, the on/off ratio decreases by one order of magnitude. In our EGOT, the SAM molecules induce a positive shift (increase) of the work function of the gate, which corresponds to a positive change of polarization of the gold electrode or, equivalently, to a shift of V_{th} to more negative values, as observed from the offset

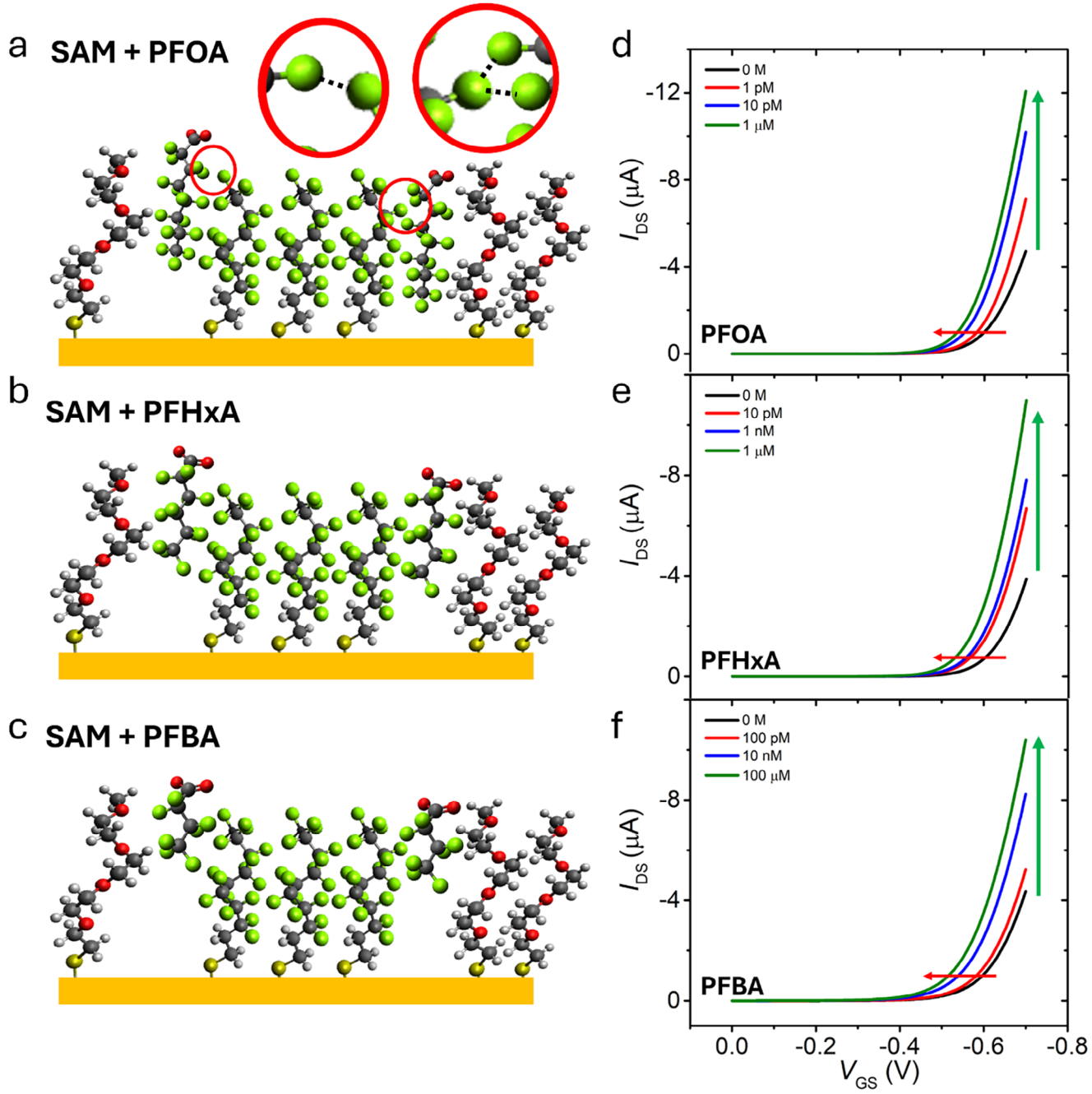

Figure 2. a–c) Schematic representation of the fluorine-fluorine interactions causing interdigitation of PFAS in the mixed SAM and PFOA (a), PFHxA (b), and PFBA (c). d–f) Transfer curves recorded at increasing concentrations of PFOA (d), PFHxA (e), and PFBA (f). Horizontal red arrow indicates the trend of the threshold voltage, green arrow the trend of the on-current vs PFAS concentration.

black curve with respect to the red one in Figure 1c. As far as the target PFAS are concerned, we selected three homolog linear pollutants, namely PFOA, PFHxA, and PFBA (Figure 1d). A standard example of the sensor response to [PFOA] is depicted in Figure 1c (blue curve): the interaction with the selected linear PFAS causes a shift of the transfer curve to less negative V_{GS}, resulting in an increase of both I_{DS} and on/off ratio proportional to [PFAS].

The interaction patterns that we expect to occur between the PFAS and the PFDT-functionalized gate electrode are schematically depicted in **Figure 2**a–c.[34–37] Manifold F···F interactions may occur as a consequence of the interdigitation of the fluorinated chains of PFAS and PFDT, thus the longest PFAS is expected to have the highest affinity for the PFDT domains. The fluorous interactions cause the variation of the polarization of the gate electrode due to the PFAS chain dipoles and

negative charges, which, synergically, make the gate electrode effectively more negative. This consideration on the electrostatic interactions is indeed confirmed by the transfer curves recorded exposing the gate to the presence of the PFAS in water and shown in Figure 2d–f, where the current I_{DS} increases with the PFAS concentration across orders of magnitude at the same applied voltages.

We assume, as shown in Figure 2a–c, that in the case of maximum chain interdigitation, the carboxylate head of the different PFAS molecules will occupy equivalent positions on the PFDT basal plane, and thus the hydrated charge should be considered the same for the three homologues. Then, the rationale for these large differences in current lies in the increasing number of fluorine-fluorine interactions that can be formed upon interdigitation. Furthermore, the amphiphilic nature of the PFAS used here (an omniphobic/fluorophilic perfluorinated chain and a hydrophilic carboxylate residue) makes the most probably accessible region for PFDT/PFAS interactions the interface between the fluorinated domains and pegylated region. In these regions, the SAM is mostly disordered due to the abrupt change in packing density and competing interactions.

It is also reasonable to assume that the interdigitation of the analytes may cause a minor reorganization of the SAM, which should not substantially affect the gate interfacial capacitance. This seems supported by the evidence that g_m does not markedly change in the curves recorded at different analyte concentrations. This observation is also supported by the measurements of electrode capacitance with electrochemical methods (Figure S3, Supporting Information). With this interpretation, we ascribe the increase of the current and the shift toward more positive threshold voltage V_{th} in the presence of PFAS to the negative charge accumulation at the interface between the gate and the electrolyte.

2.3. EGOT Response Analysis: The Dose Curves

The EGOT response to the different PFAS molecules is analyzed *vs* [PFAS] by means of two transistor parameters: the linear transconductance and either the threshold voltage V_{th} in Equation 1 (this is the standard linear analysis of the FET) or the switch-on voltage V_T in Equation 4 with the recently proposed framework.[26] The latter yields a robust estimation of V_T and provides the connection between the physical parameters of the organic semiconductor and the signal amplification due to the transistor architecture. While both the switch-on voltage V_T and V_{th} are related to the work function of the gate electrode, the two parameters differ in the definition. V_{th} derives from the conventional metal oxide-semiconductor field-effect transistors theory, but it poorly describes the physics of organic transistors. Herein, its definition is approximated as the onset voltage for the accumulation of charge carriers in the channel. Conversely, we treat V_T as the fitting parameter that represents the gate voltage at which the (semi)conductor film is in the charge neutrality condition.[26] We demonstrate that the relative variation of the output current scales as the switch-on voltage shift DV_T. By assuming that DV_T is proportional to the coverage of adsorbed PFAS, and hence to the PFAS concentration in solution, a suitable equilibrium isotherm curve explains the trend of the observed current variation.

2.4. Analysis of the Linear Regime of the Transfer Curves

As shown in **Figure 3a**, ΔV_{th} increases toward more positive values as the concentration of PFAS increases. The increasing logarithmic trend is interrupted above a characteristic concentration to yield a saturation plateau. We notice that the ΔV_{th} trends obtained for different PFAS exhibit increasing slopes according to PFOA>PFHxA>PFBA. This observation suggests that ΔV_{th} is related to the change of the chemical potential of binding and that the strength of the interaction increases with the length of the PFAS chains. The data also hint that the same plateau value is attained for all PFAS.

To rationalize the sensor response and disentangle the effect of each PFAS, we calculate the sensor signal (S) as $S_{\mathrm{PFAS}}(V_{GS},[\mathrm{PFAS}]) = \frac{I_{DS}(V_{GS},[\mathrm{PFAS}])-I_{DS}(V_{GS},0)}{I_{DS}(V_{GS},0)}$ at fixed V_{GS} value. The signal is the relative variation of I_{DS} with respect to the current response of the same device with no PFAS in solution. The dose curves for every PFAS analyte calculated at $V_{GS} = -0.7$ V are shown in Figure 3b. One immediately notices that for any PFAS there is a range where the EGOT responds monotonically, followed by a saturation plateau above a characteristic concentration. All PFAS signal curves exhibit a similar shape, albeit with marked differences: the plateau value S_{max} and the slope of the signal decreases in the order PFOA>PFHxA>PFBA; the characteristic concentration from monotonically scaling to plateau, instead, follows the opposite trend, *viz*. PFOA<PFHxA<PFBA. The latter observation hints to a greater affinity constant between the functionalized gate and PFAS with longer perfluorinated chain.

To discuss the quantitative aspects, we fit the experimental data in Figure 3a,b using the uniform Langmuir model (ULM):[38,39]

$$\Delta V_{th}([\mathrm{PFAS}]) = \frac{\Delta V_{th,max}}{2A} \cdot \ln\left(\frac{1 + K_{avg,0}e^{A}[\mathrm{PFAS}]}{1 + K_{avg,0}e^{-A}[\mathrm{PFAS}]}\right) \quad (2)$$

for the threshold voltage, and

$$S_{\mathrm{PFAS}}(V_{GS},[\mathrm{PFAS}]) = \frac{S_{max}(V_{GS})}{2A} \cdot \ln\left(\frac{1 + K_{avg}(V_{GS})e^{A}[\mathrm{PFAS}]}{1 + K_{avg}(V_{GS})e^{-A}[\mathrm{PFAS}]}\right) \quad (3)$$

for the signal.

Compared to the standard Langmuir model, which describes a single equilibrium interaction, the ULM introduces a population of binding sites with a distribution of binding energies (U) spreading across a range $\Delta U = U_{\max}-U_{\min}$. The variability of binding energies is embedded in the coefficient A of Equations 2 and 3, which is defined as $A = \frac{(U_{max}-U_{min})}{2\,k_B T}$, k_B is Boltzmann constant, T is the temperature. We find that the relevant values for our datasets are $A > 1$, which means the energy disorder is greater than twice the thermal energy, *ca* 5 kJmol^{-1}. From the best fit of the data with Equations 2 and 3, we extracted the average affinity constant K_{avg} for the SAM/PFAS interaction, the dimensionless parameter A, and S_{max}. From Taylor series expansion of Equation 3, one demonstrates that the slope at concentration [PFAS] much smaller than $1/K_{avg}(V_{GS})$ scales as $K_{avg}(V_{GS})[\frac{\sinh(A)}{A}]$. Although K_{avg} is greater for PFOA>PFHxA>PFBA, the energy spread A correlates with the inverse inequality PFOA<PFHxA<PFBA, thus the slopes of the curves tend to be comparable at low concentrations. We find that,

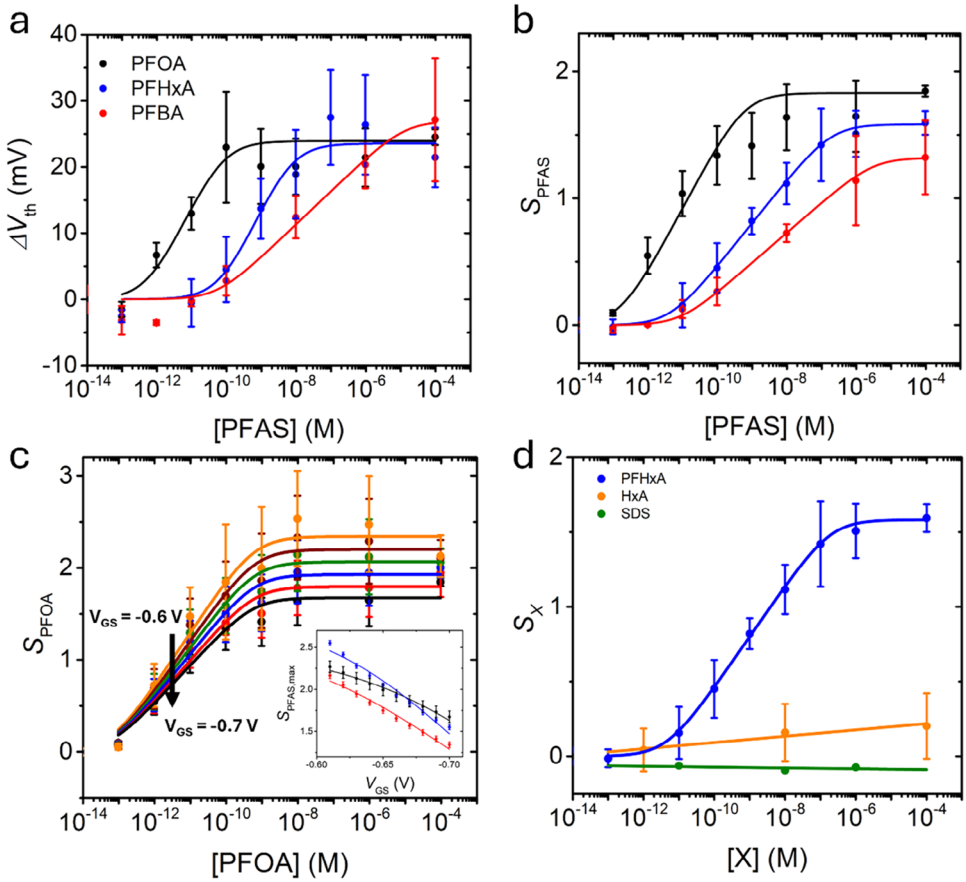

Figure 3. a) Threshold voltage shift versus PFAS molar concentration. Each color corresponds to a PFAS according to the legend. b) Dose curve built from I_{DS} signal at V_{GS} = −0.7 V versus PFAS molar concentration. Same color code as in (a). c) Dose curves of PFOA at different V_{GS} from −0.6 V (orange curve) to −0.7 V (black curve). Black arrow indicates the shift of the signal at constant concentration. Data for each PFAS are fit with Equations 2 and 3. Inset: S_{max} variation along V_{GS} is depicted. The different colors are as in (a). The continuous lines are guide to the eye obtained by fitting S_{max} data vs V_{GS} with Equation 5. d) Control experiments: comparison between the signal after the interaction with of PFOA (blue), with the non-fluorinated surfactant SDS (dark green), and with a non-fluorinated carboxilic acid hexanoic acid (HxA) (orange). The error bars correspond to the standard error of the mean (SEM) of four independent sensing experiments and two control experiments (HxA).

in general, the values of the parameter A are comparable for the two analyses, while the values of the affinity constant in Equation 2 does not depend on V_{GS}while it does in Equation 3. The latter gate voltage dependence is discussed below.

Following the IUPAC definition,[40] and on the basis of the ULM fitting curves, we calculate a limit of detection (LOD) as low as 97 fM for PFOA (0.04 ppt), 3.9 pM for PFHxA (1.2 ppt), and 11.9 pM for PFBA (2.5 ppt). These values are within the requested LODs of the techniques that are suitable for the PFAS detection requirements of the new EU regulation on water pollutants, and close to those contained in the US-EPA guidelines.[7,9,10]

Figure 3c shows some of the dose curves obtained at different values of V_{GS}.[20,41–43] While the curves retain the same shape, the increase of the modulus of the gate voltage V_{GS} yields a decrease of both K_{avg} and S_{max} in Equation 3. The **inset of** Figure 3c shows the inverse V_{GS} dependence of S_{max}, which is well represented by the trend described by Equation 5 below. The K_{avg} values extracted at three different V_{GS} from the best fit with Equation 3 are reported in Table S1 (Supporting Information), together with the fit parameters of Figure 3a (which do not exhibit a V_{GS} dependence). It is apparent how PFAS of increasing length interact more strongly with the functionalized gate electrode surface, which results into the values of the association constants K_{avg} increasing by three orders of magnitude from PFBA to PFOA. These large differences must depend on the chain length of the PFAS analyzed: the fluorine-fluorine interactions can be reasonably regarded as proportional to the number of F···F contacts, hence to the number of -CF_2- units in the molecular chains.

As control experiments, we assess the response of the EGOT to nonspecific interactions using Sodium-Dodecyl-Sulfonate (SDS), which is a nonfluorinated surfactant, and hexanoic acid (HxA), i.e. the non-fluorinated homologous of PFHxA, as target molecules. As shown in Figure 3d (green line), the interaction between the functionalized gate electrode and SDS in solution does not affect the device response, even at high concentrations, as the signal dose curve of the device is flat and negative (the current slightly decreases in the presence of SDS). We also notice the weak increasing trend of the signal (orange line) for nearly eight-decade concentration range of HxA. A comparable non-specific response is obtained using a gate electrode functionalized

with pure OEG SAM for the detection of PFBA (Figure S4, Supporting Information), thus the non-specific signals are probably caused by a weak interaction between the carboxylic residues of the molecules in solution and the OEG domains of the SAM. As a further control, we monitor the variation of the electrical response of the EGOT before and after the sensing experiment, using as a control gate a bare gold electrode (Figure S5, Supporting Information). As evident, the performance of the device slightly worsens, resulting in a shift of the threshold voltage to more negative V_{GS} and a decrease of the output current I_{DS}. This effect is opposite and decisively lower in magnitude than the variation due to the sensing of the tested PFAS molecules.

2.5. Correlation Between Current Signal and Switch on Voltage Shift

We now analyze the EGOT transfer curves according to the model and the protocol that we recently proposed to unify the chemical-physical description of EGOFET and OECT.[26] This framework allows us to reproduce the whole transfer curve and to obtain reliable and robust values of the EGOT sensor characteristic parameters.

We recall the analytical expression for the EGOT current that describes the transfer curves across the whole gate voltage range:[26]

$$I_{DS}\left(V_{GS};\ V_{DS};[\mathrm{PFAS}]\right) \approx I_{DS,off}\left(V_{DS}\right) + g_{m,l}\left(V_{DS}\right)\left\{\frac{\alpha\sigma}{e}\frac{sinh\left(2e\frac{V_{GS}-V_T}{\sigma}\right)-sinh\left(e\frac{V_{GS}-V_T}{\sigma}\right)}{sinh\left(\frac{\varepsilon}{\sigma}\right)+\alpha\ cosh\left(2e\frac{V_{GS}-V_T}{\sigma}\right)}\right\} \quad (4)$$

Here $I_{DS,off}(V_{DS})$ is the EGOT off-current; $g_{m,l} = \frac{W}{L}\mu C_{DL}\ V_{DS}$ is the linear transconductance of the EGOT device (alike the one extracted from the linear part of the transfer curve); e is the elementary charge; V_T is the switch-on voltage (surrogating the role of the threshold voltage V_{th} of the linear regime analysis); σ and ε are two energy parameters of the organic semiconductor: the former measures the energy disorder in the gap, while ε is half of the HOMO-LUMO band gap (estimated as distance between the band edges of an organic semiconductor with exponential disorder). The dimensionless ratio of areal charge densities $\alpha = (\frac{2en_{max}d}{C_{DL}\sigma/e})$ depends on the maximum areal number density of electrons $2n_{max}d$ that can populate the tail of the density of states in the bandgap ($2n_{\max}$), and on the organic semiconductor thin film thickness d. The interfacial capacitance C_{DL} encompasses both the gate and the channel interfacial capacitances in series, hence is sensitive, in principle, to the molecular composition of the gate, i.e., to the PFAS coverage (fraction of occupied binding sites) at the gate.

Equation 4 embodies the voltage-dependent effective capacitance that generates the charge carriers in the channel. In the EGOT sensor, the three parameters affected by the analyte concentration are, in principle, the voltage V_T, the transconductance $g_{m,l}$ and α. The voltage V_T is influenced by the PFAS concentration [PFAS], since the PFAS coverage is proportional to [PFAS], and the electrostatic energy at the gate-electrolyte interface changes with the PFAS coverage. The transconductance $g_{m,l}$ and the parameter α are associated with the possible variation of the interfacial capacitance with [PFAS]. We assume that the properties of the organic semiconductor thin film, and hence the parameters σ and ε, in this experiment are insensitive to PFAS concentration and will be treated as fixed global parameters.

In **Figure 4a**, we show the results of the best fit of the transfer curves acquired at different concentrations of PFOA in water using Equation 4. Based on experimental evidence (Figure S3, Supporting Information), we observe that the concentration effect is more significant on V_T than in the other parameters. Therefore, we fit the whole individual transfer curves for the three homolog PFAS with Equation 4, using the energy disorder σ, α and the transconductance $g_{m,l}$ as concentration-independent global parameters, with a fixed band gap for DPP-DTT of $2\varepsilon = 1.7$ eV.[44] The baseline off current $I_{DS,off}(V_{DS})$ is also fixed to its average value. The continuous lines overlayed to the dotted transfer curves in Figure 4a represent the fit to the experimental curves with this model. When the gate voltage of each transfer curve is shifted by its value of V_T, the set of the transfer curves collapse into a 'universal' transfer curve shown in the inset of Figure 4a. This reinforces the hypothesis that V_T is the parameter more affected by PFAS binding at the gate electrolyte interface.

In Figure 4b, we show the trend of the best-fit value of switch-on voltage shift $\Delta V_T = V_T([PFAS]) - V_{T,SAM}$ for the three homolog PFAS. $V_{T,SAM}$ is the switch-on voltage with the functionalized gate in the absence of PFAS. ΔV_T is larger for PFOA>PFHxA>PFBA at the low concentrations and saturates to the same plateau value ~80 mV at the larger concentrations. We notice that taking into account the intervals of confidence around the lines of best fit (the ones drawn are for 95% confidence level) the PFOA curve is already distinct from the others for concentrations as low as 1 pM, whereas PFHxA and PFBA become separated by their confidence intervals for concentrations ≈1 nM.

The shifts of the threshold voltage V_{th} obtained from Equation 1 (Figure 3a) are always smaller than those of the switch-on voltage V_T obtained from Equation 4. For instance, ΔV_T ranges up to 80 mV, while ΔV_{th} ranges up to 25 mV, thus making the sensitivity of ΔV_T to the PFAS concentration about three times larger than the one of ΔV_{th}, This is clear from the linear correlation plot between ΔV_{th} and ΔV_T shown in the inset of Figure 4b. Noticeably, the standard errors of the mean (SEM) on ΔV_T are smaller than the ones on ΔV_{th}.

We are now able to analyze the sensor signal $S(V_{GS};[PFAS])$. Because of the insensitivity of the interfacial capacitance C_{DL} to the concentration of PFAS, and assuming that the baseline currents $I_{DS,off}(V_{DS})$ are negligible with respect to the EGOT current, a condition which applies for $|V_{GS} - V_T| > \sigma/e$, the signal turns out to be independent of the transconductance $g_{m,l}$:

$$S\left(V_{GS};\ [\mathrm{PFAS}]\right) \approx \left\{\left\{\frac{\sinh\left(2\left(\nu_{SAM}-\Delta\nu_T\right)\right)-\sinh\left(\nu_{SAM}-\Delta\nu_T\right)}{\sinh\left(2\nu_{SAM}\right)-\sinh\left(\nu_{SAM}\right)}\right\} \times \left\{\frac{\sinh\left(\frac{\varepsilon}{\sigma}\right)+\alpha\ \cosh\left(2\nu_{SAM}\right)}{\sinh\left(\frac{\varepsilon}{\sigma}\right)+\alpha\ \cosh\left(2\left(\nu_{SAM}-\Delta\nu_T\right)\right)}\right\}-1\right\} \quad (5)$$

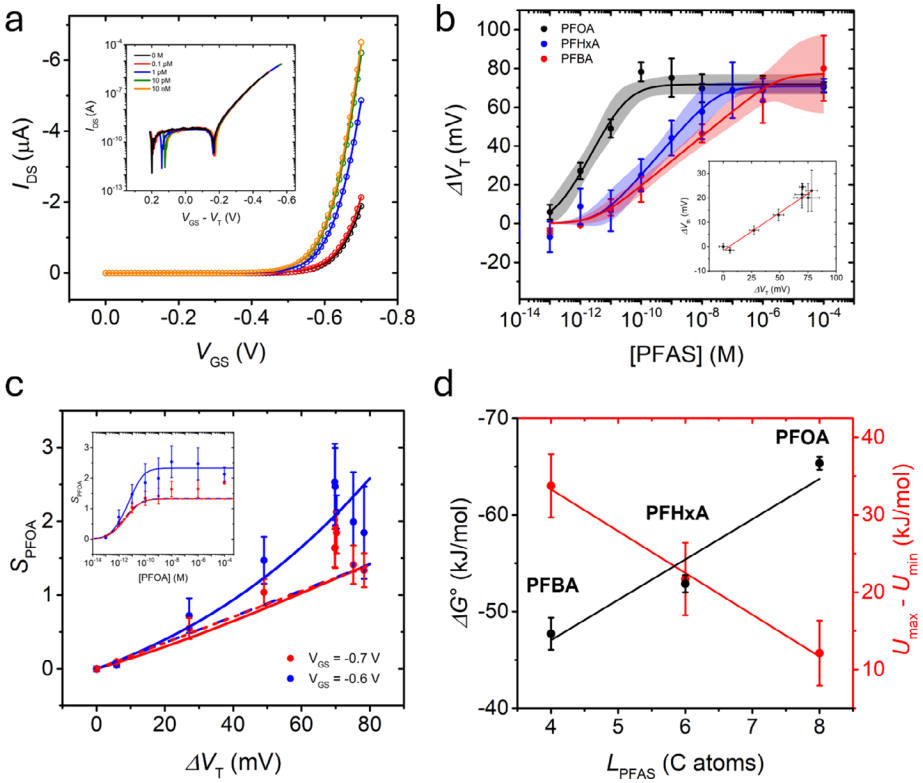

Figure 4. a) Representative transfer curves (dots) for PFOA fitted with Equation 4 (continuous lines). In the inset the same transfer curves plotted against V_{GS}-V_T overlapping onto a universal transfer curve (semilog graph). b) PFAS concentration dependence of ΔV_T, estimated from at least four different dataset per point are plotted against the PFAS concentrations with the standard error of the mean, the shaded areas confidence interval of the fit equation (ULM), selecting a confidence level of 95 %; in the inset: correlation plot between ΔV_T (horizontal axis) and ΔV_{th} (vertical axis). The first one is about three times the latter, as the red line slope is 0.31 ± 0.02. c) S_{PFOA} versus ΔV_T at two different V_{GS} and the corresponding Equation 5 (continuous lines) and Equation 6 (dashed lines). In the inset S_{PFOA} versus [PFOA] at 2 different V_{GS} and the corresponding Equation 5 (continuous lines) and Equation 6 (dashed lines), where the dependency of ΔV_T on PFBA concentration is described by the corresponding Uniform Langmuir Model isotherm. d) standard free energy of binding ΔG° calculated from the averaged association constant (black) and the energy spread ΔU (red) plotted against the PFAS length. Both properties are calculated from the best fit value of ΔV_T versus PFAS concentration and its linear fit.

Here we introduce the dimensionless effective gate voltage of the SAM functionalized electrode $v_{SAM} = \frac{V_{GS}-V_{T,SAM}}{\sigma/e}$ and the dimensionless gate voltage shift $\Delta v_T = \frac{\Delta V_T([\text{PFAS}])}{\sigma/e}$. As $\frac{\varepsilon}{\sigma} \approx 6.7 > 1$ the second factor will approach $\frac{1+\alpha exp(\frac{2e|V_{GS}-V_{T,SAM}|-\varepsilon}{\sigma})}{1+\alpha exp(\frac{2e|V_{GS}-V_{T,SAM}-\Delta V_T|-\varepsilon}{\sigma})} \approx 1$ for $\Delta v_T \ll 1$. Under these conditions the signal can be approximated as:

$$S\left(V_{GS};\ [\text{PFAS}]\right) \approx \left\{\frac{e}{\sigma}\frac{cosh\left(v_{SAM}\right)-2cosh\left(2v_{SAM}\right)}{sinh\left(2v_{SAM}\right)-sinh\left(v_{SAM}\right)}\right\}\Delta V_T\left([\text{PFAS}]\right) \quad (6)$$

Within this limit, the signal will no longer exhibit a dependence on α and ε. We can identify the factor in curly brackets as an amplification factor which depends on the value v_{SAM}: for negative values, it is positive and greater than or equal to 2 (the asymptotic value at large negative values).

For $v_{SAM} \to 0$ Equation 6 reads as $S(V_{GS};\ [\text{PFAS}]) \approx -\frac{\Delta V_T([\text{PFAS}])}{V_{GS}-V_{T,SAM}} = -\frac{\Delta V_T([\text{PFAS}])}{v_{SAM}}$. Therefore, Equation 6 predicts that the signal will decrease for $V_{GS} - V_{T,SAM} \ll 0$, and that the EGOT operation at low gate voltage yield the largest signal, since the signal decreases inversely with the gate voltage in agreement with the **inset of** Figure 3c.

We also notice that the saturation plateau will be related to the plateau $\Delta V_{T,max}$ as $S_{max}(V_{GS}) \approx \{\frac{e}{\sigma}\frac{cosh(v_{SAM})-2cosh(2v_{SAM})}{sinh(2v_{SAM})-sinh(v_{SAM})}\}\Delta V_{T,max}$. Since $\Delta V_{T,max} \approx 80$ mV for all the investigated PFAS, the origin of the different signal plateaus S_{max} for each PFAS arises from the device properties within the curly brackets in Equation 6.

2.6. Concentration Dependence of the Current Signal and the Switch on Voltage Shift

The good qualitative agreement with our prediction and experimental data spurs us to test quantitatively Equations 5 and 6. First, in Figure 4c, we plot both theoretical (continuous and dashed lines as Equations 5 and 6, respectively) and experimental (symbols) dependency of S_{PFOA} on ΔV_T. We plug into the equations the average best fit parameters (σ, α, ε and v_{SAM}) from the analysis of the EGOT sensors used for PFOA detection with

Equation 4 (their values are reported in Table S3, Supporting Information). Equation 5 describes accurately the S_{PFOA} trend on ΔV_T at both the gate potentials. Approximation in Equation 6 instead works nicely at $V_{GS} = -0.7$ V for all ΔV_T, and at $V_{GS} = -0.6$ V at small ΔV_T, while deviates substantially at high ΔV_T for $V_{GS} = -0.6$ V. This is consistent with the assumptions behind Equation 6.

We extend now the considerations above to the dependence on [PFAS].

We recast Equations 5 and Equation 6 replacing ΔV_T with its dependency on [PFAS], which, similarly to Equation 2 is described by $\Delta V_T([\text{PFAS}]) = \frac{\Delta V_{T,max}}{2A} \cdot \ln\left(\frac{1+K_{avg,0}e^{A}\,[\text{PFAS}]}{1+K_{avg,0}\,e^{-A}\,[\text{PFAS}]}\right)$. The best fit values $K_{avg,0}$, A and $\Delta V_{T,max}$ are extracted from the data in Figure 4b. In the inset of Figure 4c, we plot the predicted S_{PFOA} (continuous and dashed lines) from Equations 5 and 6, and experimental S_{PFOA} defined at two different gate potentials vs [PFOA]. Remarkably, Equation 5 reproduces perfectly the dependency of S_{PFOA} vs [PFOA] for the two V_{GS} values. Instead, Equation 6 (dashed lines) predicts correctly S_{PFOA} vs [PFOA] for $V_{GS} = -0.7$ V, while fails to predict the trend for $V_{GS} = -0.6$ V.

At this point, considering that all the measurements are conducted at (quasi)equilibrium, we can infer the thermodynamics of the interaction between PFAS and the mixed SAM from the ULM isotherm that describes the ΔV_T variation vs [PFAS] as in the fit of Figure 4b.

While $\Delta V_{T,max}$ is the same for the three different PFAS, consistently with the hypothesis that the three PFAS have the same number of possible interaction sites, K_{avg} and A change as function of PFAS length (L_{PFAS}). Thus, the selectivity of the sensor toward different linear PFAS stems from these parameters. In Figure 4d, we plot the chain-length dependence L_{PFAS} of the standard Gibbs free energy $\Delta G° = -RT\,ln\,K_{avg,0}$ of the interaction between PFAS and the binary SAM, together with and the energy dispersion ΔU between the different interaction sites. We take the laboratory temperature 293.15 K. The $\Delta G°$ values are the following: PFOA = −65.3 ± 0.7 kJ mol^{-1}, PFHxA = −52.9 ± 0.9 kJ mol^{-1} and PFBA = −48 ± 2 kJ mol^{-1}. We notice the linear correlation between ΔG^0 and L_{PFAS}, which hints to free energy of binding proportional to the number of perfluorinated carbon units. Interestingly, the rate of increase of ΔG^0 is 4 ± 1 kJ mol^{-1} per unit, which suggests that for an increase of two units in the PFAS chain, there are one or two additional F···F interactions established (see schematics in Figure 2a) as earlier references report 2–3 kJ mol^{-1} for a single F···F bond.[34,35] These values confirm that our sensor can distinguish two species of homolog linear series when the difference in chain length is either one or two —CF_2- units. These considerations explain why the interaction energy is lower for PFBA than for PFHxA and PFOA. Additional evidence supporting the role of fluorine-fluorine interactions as driver for PFAS recognition is the energy dispersion ΔU, which decreases with PFAS length symptomatic of lesser energy fluctuations as the binding energy becomes much larger than thermal energy.

The demonstration that EGOT is able to resolve binding energy differences one-two times the thermal energy is a remarkable outcome. This figure of merit clearly indicates a strategy for the selective quantification and identification of different PFAS: a suitable design of a perfluorinated recognition species for each class of PFAS, either linear, branched, dendritic, and/or with more complex geometries should be envisioned for fabricating arrays of EGOT sensors capable of classifying the species in water.

2.7. Test in Real Matrices

We finally assessed our EGOT sensor on a real matrix, *viz*. bottled water spiked with PFHxA. An example of transfer curves registered at increasing [PFHxA] is reported in **Figure 5**a. Using ΔV_T as the observable parameter, we build the dose curve reported in Figure 5b (red markers) and overlay them with the sensing response previously obtained in distilled water (blue markers and line). The two data sets are in good agreement, albeit the response of the device in bottled water seem influenced by the presence of ions (reported in Table S2, Supporting Information) interacting with the SAM, thus resulting in larger error bars. The horizontal shifts of the red markers with respect to the "ideal" dose curve (blue line) at concentrations much higher than the 3.9 pM LOD will lead to underestimate the real concentration by a factor ca. 4-5 above 1 nM, and to overestimate it by the same factor. These results confirm the efficacy of our device toward PFAS, and sug-

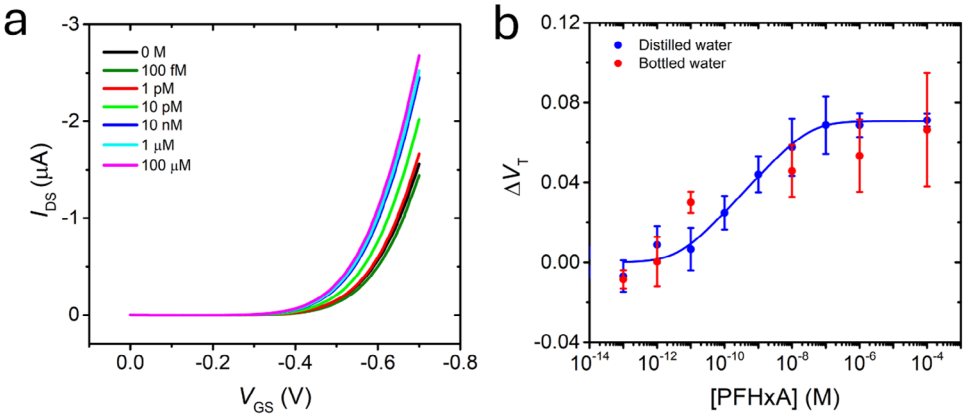

Figure 5. a) Transfer curves recorded at increasing [PFHxA] in bottled water. b) PFHxA dose curves as variation of V_T in distilled water (blue points) and bottled water (red points). The error bars correspond to the standard error of the mean (SEM).

gest that a proper rescaling may lead to map different aqueous solutions onto a universal curve.

3. Conclusion

This first-ever label-free EGOT sensor for PFAS exploits a tailored perfluorinated interface to specifically detect and selectively quantify PFAS in water. Limits of detection (LOD) as low as 97 fM for PFOA (0.04 ppt), 3.9 pM for PFHxA (1.2 ppt), and 11.9 pM for PFBA (2.5 ppt) were obtained, which are within the state-of-the-art parameters set by current water preservation and environmental authorities. The LOD exhibited by the EGOT on PFOA is about three orders of magnitude smaller than the parameter indicated by the EU Directive. The specificity and selectivity arise from the fluorophobic partition of the target PFAS molecules binding to the fluorinated domains of the gate SAM, thanks to manifold fluorine-fluorine interactions. The functionalization of the gate electrode with our mixed oligoethyleneglycol/perfluoroalkane SAM is robust and reproducible. The model used for data interpretation allowed us to rationalize the quantitative differences between different PFAS in terms of their interaction mechanism via fluorine-fluorine interactions with the SAM. In particular, we found that each $-CF_2-$ unit of the target PFAS contributes -4 kJ mol^{-1} to the binding energy, thus, the proposed sensor in principle resolves linear PFAS with chain lengths differing by one perfluoro-methylene unit, whose interaction difference is less than twice the thermal energy *RT*. Interestingly, the EGOT sensor gives information about the thermodynamics of the interactions, which is also useful to better understand the behavior of PFAS at interfaces.

The sensor herein demonstrated is designed for in-field deployed applications, thus, it is suitable for on-site detection of aqueous PFAS at the sub-ppt level. The response is obtained in less than 10 min, with minimal sample preparation, and straightforward measurements. The sensing strategy described here can be readily applied to any linear PFAS, and with further molecular design of the perfluorinated SAM-forming species, can be repurposed toward more complicated molecular structures, thus opening the way to label-free sub-ppt detection of a variety of perfluorinated pollutants in water. Preliminary results with PFAS-spiked solutions in bottled water hint that our results may be transferred to real water samples without excessive effort.

4. Experimental Section

Reagents: The gold wires used as gate electrodes and working electrodes have 1 mm of diameter.

The interdigitated source and drain electrodes (substrates) are supplied by Micrux (Spain), they are the model ED-IDE1-Au: gold on glass, 90 pairs of interdigitated gold electrodes, dimensions $10 \times 6 \times 0.75$ mm, electrodes width 10 µm, gap width 10 µm.

2,5,8,11-Tetraoxatridecane-13-thiol (OEG) is produced by PurePEG LLC (USA).

Perfluorodecanethiol (PFDT), sodium-dodecyl-sulphate (SDS), hexanoic acid (HA), KCl, KOH, H_2SO_4, and $K_3Fe(CN)_6$ are acquired from Sigma–Aldrich (Germany).

Standardized PFOA, PFHxA and PFBA are titrated with NMR prior the measurements.

Poly[2,5-(2-octyldodecyl)-3,6-diketopyrrolopyrrole-alt-5,5-(2,5-di(thien-2-yl)thieno[3,2-b]thiophene)] (DPP-DTT) with MW = 111 kDa is produced by Ossila (UK).

Device Fabrication: First, the substrate (ED-IDE1-Au by Micrux, Spain) should be cleaned. The cleaning procedure consists of 10 min of sonication in Hellmanex 1%, 10 min of sonication in distilled water, and 10 min of sonication in ethanol.[45] The DPP-DTT solution is made by heating a solution of 5 mg mL^{-1} of DPP-DTT in 1,2-dichlorobenzene at 80 °C for 1 h. 10 µl of DPP-DTT heated solution was deposited over the substrate to form an organic semiconductor layer channel by spin-coating. The spinning procedure consists of 2 min at 2000 rpm, with an acceleration of 100 rpm s^{-1}. Then, the device was heated at 140 °C for 30 min to cure the semiconductor layer.

The gold wire used as gate electrode is cleaned by 4 h of immersion in KOH 2.5 M at 120 °C, and 2 h of immersion in H_2SO_4 concentrated at 220 °C. Then it was rinsed by water and ethanol, and it was dipped for 16 h at 20 °C in an ethanol solution of OEG (PurePEG LLC, USA) 3 mM and PFDT (Sigma–Aldrich, Germany) 1 mM. After the functionalization the gold wire was rinsed with ethanol, and it was left in distilled water for 1 h.

To perform the capacitive coupling between the gate electrode and the semiconductive channel a drop of distilled water (50 µl) was deposited between the two elements.

Electrical Characterization: All electrical measurements were performed using a Precision Source/Measure Unit (SMU) Agilent B2912A. The transfer curves were recorded maintaining constant the voltage difference between the source electrode and the drain electrode (V_{DS} = −0.1 V) and sweeping the voltage difference between the gate electrode and the source electrode (V_{GS}) between 0 and −0.7 V. Each measure was conducted until a stable transfer curve was recorded. Before the sensing experiment, the device was switched on and off until reaching a stable response (Figure S6, Supporting Information).

To register a dose curve, the same functionalized gate was incubated in analyte solutions at increasing concentrations for 10 min, ex situ. After incubation, before the electrical characterization, the gate electrode was rinsed with water (distilled or bottled). For the three PFAS molecules tested, the data reported are the average of four independent sensing experiments.

Electrochemical Characterization: It is conducted in a standard electrochemical cell, in a three electrodes set-up using a CHI-760D potentiostat from CH-Instrument. The three electrodes are the gold wire as working electrode (WE), an Ag/AgCl reference electrode (RE), and a platinum counter electrode (CE). The electrochemical cell is filled by a solution of $Fe(CN)_6^{4-/3-}$ 5 mM and KCl 1 M. Two techniques were applied, the electrochemical impedance spectroscopy (EIS) and the cyclic voltammetry (CV). To perform the CV the potential difference is swept between −0.2 V vs Ag/AgCl and 0.6 V vs Ag/AgCl. The EIS is conducted at the half-wave potential sweeping the frequency between 0.1 and 100 000 Hz. To measure the capacitance of the working electrode the CV were recorded in a solution of KCl 0.1 M.

Spiked Solutions Characterization: High performance liquid chromatography mass spectrometry (HPLC-MS) was adopted to validate the concentration of PFAS in the spiked solutions, which resulted in the right order of magnitude.

Supporting Information

Supporting Information is available from the Wiley Online Library or from the author.

Acknowledgements

P.M. and F.B. contributed equally to this work. F.B. dedicates this work in memoriam of Prof. Paolo Biscarini. This work was supported by the Italian Ministry of Research through the project "NiFTy" (PRIN2017, Grant

No. 2017MYBTXC) and conducted within the Technologies of Sustainability Flagship of the Istituto Italiano di Tecnologia. M.B. acknowledges the Life Sciences Department for the grant "FAR 2021". M.S. acknowledges co-financing from the European Union - FSE-REACT-EU, PON research and Innovation 2014-2020 DM1062/2021. The research leading to these results has received also funding from the European Union – NextGenerationEU through the Italian Ministry of University and Research under PNRR – M4C2-I1.3 Project PE_00000019 "HEAL ITALIA" to Carlo Augusto Bortolotti, Marcello Berto, and Matteo Sensi. The views and opinions expressed are those of the authors only and do not necessarily reflect those of the European Union or the European Commission. Neither the European Union nor the European Commission can be held responsible for them.

Conflict of Interest

The authors declare no conflict of interest.

Data Availability Statement

The data that support the findings of this study are available from the corresponding author upon reasonable request.

Keywords

affinity constant, EGOT, environmental monitoring, fluorinated pollutants, self-assembled monolayer

Received: April 3, 2025
Revised: June 11, 2025
Published online:

[1] X. Lim, *Nature* **2023**, *620*, 24.
[2] K. Sznajder-Katarzyńska, M. Surma, I. Cieślik, *J. Chem.* **2019**, *2019*, 1.
[3] E. Panieri, K. Baralic, D. Djukic-Cosic, A. Buha Djordjevic, L. Saso, *Toxics* **2022**, *10*.
[4] S. E. Fenton, A. Ducatman, A. Boobis, J. C. DeWitt, C. Lau, C. Ng, J. S. Smith, S. M. Roberts, *Environ. Toxicol. Chem.* **2021**, *40*, 606.
[5] S. C. E. Leung, D. Wanninayake, D. Chen, N.-T. Nguyen, Q. Li, *Sci. Total Environ.* **2023**, *905*, 166764.
[6] J. P. Giesy, K. Kannan, *Environ. Sci. Technol.* **2001**, *35*, 1339.
[7] *Directive (Eu) 2020/2184 of the European Parliament and of the Council of 16 December 2020 on the quality of water intended for human consumption, OJ L 435, 23.12.2020*, pp. 1–62.
[8] OECD (2021), Reconciling Terminology of the Universe of Per- and Polyfluoroalkyl Substances: Recommendations and Practical Guidance, OECD Series on Risk Management of Chemicals, OECD Publishing, Paris.
[9] *US-EPA (2022), Lifetime Drinking Water Health Advisories for Four Perfluoroalkyl Substances (PFAS), Environmental Protection Agency (FRL 9855-01-OW)*.
[10] *US-EPA (2022), SW-846 Test Method 8327: Per-and Polyfluoroalkyl Substances (PFAS) by Liquid Chromatography/Tandem Mass Spectrometry (LC/MS/MS), Environmental Protection Agency (SW-846)*.
[11] G. L. Glish, R. W. Vachet, *Nat. Rev. Drug Discov.* **2003**, *2*, 140.
[12] A. U. Rehman, M. Crimi, S. Andreescu, *Trends Environ. Anal. Chem.* **2023**, *37*, 00198.
[13] M. Takayose, K. Akamatsu, H. Nawafune, T. Murashima, J. Matsui, *Anal. Lett.* **2012**, *45*, 2856.
[14] H. Niu, S. Wang, Z. Zhou, Y. Ma, X. Ma, Y. Cai, *Anal. Chem.* **2014**, *86*, 4170.
[15] R. Kazemi, E. I. Potts, J. E. Dick, *Anal. Chem.* **2020**, *92*, 10597.
[16] Y. H. Cheng, D. Barpaga, J. A. Soltis, V. Shutthanandam, R. Kargupta, K. Sung Han, B. P. McGrail, R. Kishan Motkuri, S. Basuray, S. Chatterjee, *ACS Appl. Mater. Interfaces* **2020**, *12*, 10503.
[17] J. Park, K.-A. Yang, Y. Choi, J. K. Choe, *Environm. Int.* **2022**, *158*, 107000.
[18] A. Concellón, J. Castro-Esteban, T. M. Swager, *J. Am. Chem. Soc.* **2023**, *145*, 11420.
[19] S. Park, C. T. Gordon, T. M. Swager, *Proc. Natl. Acad. Sci. U. S. A.* **2024**, *121*, 2317300121.
[20] M. Berto, S. Casalini, M. Di Lauro, S. L. Marasso, M. Cocuzza, D. Perrone, M. Pinti, A. Cossarizza, C. F. Pirri, D. T. Simon, M. Berggren, F. Zerbetto, C. A. Bortolotti, F. Biscarini, *Anal. Chem.* **2016**, *88*, 12330.
[21] M. Larisika, C. Kotlowski, C. Steininger, R. Mastrogiacomo, P. Pelosi, S. Schütz, S. F. Peteu, C. Kleber, C. Reiner-Rozman, C. Nowak, W. Knoll, *Angew. Chem., Int. Ed.* **2015**, *54*, 13245.
[22] S. P. White, S. Sreevatsan, C. D. Frisbie, K. D. Rapid Dorfman, *ACS Sens.* **2016**, *1*, 1213.
[23] M. Sensi, R. F. de Oliveira, M. Berto, A. Paradisi, P. Greco, C. A. Bortolotti, P. Samorì, F. Biscarini, *Adv. Funct. Mater.* **2024**, *34*, 2313871.
[24] E. Macchia, K. Manoli, B. Holzer, C. Di Franco, M. Ghittorelli, F. Torricelli, D. Alberga, G. F. Mangiatordi, G. Palazzo, G. Scamarcio, L. Torsi, *Nat. Commun.* **2018**, *9*, 3223.
[25] V. Percec, M. Glodde, G. Johansson, V. S. K. Balagurusamy, P. A. Heiney, *Angew. Chem., Int. Ed.* **2003**, *42*, 4338.
[26] R. Zanotti, M. Sensi, M. Berto, A. Paradisi, M. Bianchi, P. Greco, C. A. Bortolotti, M. Di Lauro, F. Biscarini, *Adv. Mater.* **2024**, *36*, 2410940.
[27] M. Baghbanzadeh, C. M. Bowers, D. Rappoport, T. Zaba, L. Yuan, K. Kang, K. C. Liao, M. Gonidec, P. Rothemund, P. Cyganik, A. Aspuru-Guzik, G. M. Whitesides, *J. Am. Chem. Soc.* **2017**, *139*, 7624.
[28] C. Gabellini, M. Sologan, E. Pellizzoni, D. Marson, M. Daka, P. Franchi, L. Bignardi, S. Franchi, Z. Posel, A. Baraldi, P. Pengo, M. Lucarini, L. Pasquato, P. Posocco, *ACS Nano* **2022**, *16*, 20902.
[29] S. Bidoggia, F. Milocco, S. Polizzi, P. Canton, A. Saccani, B. Sanavio, S. Krol, F. Stellacci, P. Pengo, L. Pasquato, *Bioconjugate Chem.* **2017**, *28*, 43.
[30] S. Trabelsi, S. Zhang, Z. Zhang, T. R. Lee, D. K. Schwartz, *Soft Matter* **2009**, *5*, 750.
[31] M. D. Marquez, O. Zenasni, A. C. Jamison, T. R. Lee, *Langmuir* **2017**, *33*, 8839.
[32] P. Pengo, M. Sologan, L. Pasquato, F. Guida, S. Pacor, A. Tossi, F. Stellacci, D. Marson, S. Boccardo, S. Prici, P. Posocco, *Eur. Biophys. J.* **2017**, *46*, 749.
[33] A. Doumbia, J. Tong, R. J. Wilson, M. L. Turner, *Adv. Electron. Mater.* **2021**, *7*, 2100071.
[34] H. Omorodion, B. Twamley, J. A. Platts, R. J. Baker, *Cryst. Growth Des.* **2015**, *15*, 2835.
[35] R. J. Baker, P. E. Colavita, D. M. Murphy, J. A. Platts, J. D. Wallis, *J. Phys. Chem. A* **2012**, *116*, 1435.
[36] A. Stergiou, L. Leccioli, D. Ricci, M. L. Zaffalon, S. Brovelli, F. Baldelli Bombelli, G. Terraneo, P. Metrangolo, G. Cavallo, *Angew. Chem., Int. Ed.* **2024**, *63*, 202408570.
[37] C. Pigliacelli, A. Acocella, I. Díez, L. Moretti, V. Dichiarante, N. Demitri, H. Jiang, M. Maiuri, R. H. A. Ras, F. Baldelli Bombelli, G. Cerullo, F. Zerbetto, P. Metrangolo, G. Cattaneo, *Nat. Commun.* **2022**, *13*, 2607.
[38] A. Paradisi, M. Berto, M. Di Giosia, S. Mazzali, M. Borsari, T. D. Marforio, F. Zerbetto, M. Calvaresi, A. Orieshyna, N. Amdursky, C. A. Bortolotti, F. Biscarini, *Chem. A Europ. J.* **2023**, *29*, 202301704.

[39] H. Swenson, N. P. Stadie, *Langmuir* **2019**, *35*, 5409.
[40] A. D. McNaught, A. Wilkinson, *IUPAC Compendium of chemical terminology. The "Gold Book"*, Blackwell Scientific Publications, Oxford, **1997**.
[41] C. Diacci, M. Berto, M. Di Lauro, E. Bianchini, M. Pinti, D. T. Simon, F. Biscarini, C. A. Bortolotti, *Biointerphases* **2017**, *12*, 05F401.
[42] X. P. A. Gao, G. Zheng, C. M. Lieber, *Nano Lett.* **2010**, *10*, 547.
[43] M. Berto, M. Di Giosia, M. Giordani, M. Sensi, F. Valle, A. Alessandrini, C. Menozzi, A. Cantelli, G. C. Gazzadi, F. Zerbetto, M. Calvaresi, F. Biscarini, C. A. Bortolotti, *Adv. Elect. Mater.* **2021**, *7*, 2001114.
[44] W. Li, W. S. C. Roelofs, M. M. Wienk, R. A. J. Janssen, *J. Am. Chem. Soc.* **2012**, *134*, 13787.
[45] M. Sensi, A. Ricci, G. Rigillo, A. Paradisi, M. Berto, N. Gnesutta, C. Imbriano, F. Biscarini, C. A. Bortolotti, *J. Mater. Chem. C* **2024**, *12*, 7596.